
GEOSPATIAL PERSPECTIVE REPROJECTIONS FOR GROUND-BASED SKY IMAGING SYSTEM

Guillermo Terrén-Serrano

Department of Electrical and Computer Engineering
The University of New Mexico
Albuquerque, NM 87131, United States
guillermoterren@unm.edu

Manel Martínez-Ramón

Department of Electrical and Computer Engineering
The University of New Mexico
Albuquerque, NM 87131, United States
manel@unm.edu

November 1, 2021

ABSTRACT

Sky imaging systems use lenses to acquire images concentrating light beams in a sensor. The light beams received by the sky imager have an elevation angle with respect to the device normal. Thus, the pixels in the image contain information from different areas of the sky within the imaging system field of view. The area of the field of view contained in the pixels increases as the elevation angle of the incident light beams decreases. When the sky imager is mounted on a solar tracker, the light beam's angle of incidence in a pixel varies over time. This investigation formulates and compares two geospatial reprojections that transform the original euclidean frame of the imager plane to the geospatial atmosphere cross-section where the sky imager field of view intersects the cloud layer. One assumes that an object (i.e., cloud) moving in the troposphere is sufficiently far so the Earth's surface is approximated *flat*. The other transformation takes into account the curvature of the Earth in the portion of the atmosphere (i.e., voxel) that is recorded. The results show that the differences between the dimensions calculated by both geospatial transformations are in the order of magnitude of kilometers when the Sun's elevation angle is below 30° .

Keywords Infrared Camera · Perspective Reprojection · Sky Imaging · Solar Forecasting; Sun Tracking

1 Introduction

The Global Solar Irradiance (GSI) that reaches the Earth's surface depends on shadows projected by moving clouds in the troposphere [1]. Consequently, clouds influence the energy generation in Photovoltaic (PV) powered smart grids. GSI forecasting methods, which are efficient for intra-hour horizons, analyze the dynamics of clouds to predict GSI minutes ahead of time using data acquired using ground-based sky imagers [2], to control the storage and dispatch of energy.

The horizons of intra-hour solar forecasting depend on the Field of View (FOV) of the sky imager used to acquire the images. A sky imager may be composed of one or multiple visible or Infrared (IR) imagers, or both, and their FOV generally varies from 60° (low) to 180° (large). However, unless the sky imager is mounted on a solar tracker [3, 4, 5], the necessary FOV to perform an accurate intra-hour solar forecast is large. Total Sky Imagers (TSI) achieved large FOV sky images using a concave mirror to reflect light beams into a visible [6] or IR camera [7], and the camera is installed on a support at the focal distance of the mirror [8, 9]. An alternative to reflective sky imagers (in visible light sky images), is to increase the camera's FOV using a fisheye lens [10, 11, 12, 13]. These are generally known as "all sky imagers" [14, 15, 16]. Similarly, the FOV of IR sky imagers can be enlarged applying image processing techniques to merge images acquired from multiple low FOV imagers [17].

Each of these sky imagers use light beams received at an angle with respect to the imager's plane. Therefore, the produced distortion should be corrected using a geometric transformation to compute the velocity vectors of a cloud. The geometric transformation proposed by [18] transforms the Euclidean coordinate system of the pixels to a coordinate system based on the azimuth and elevation angles. This transformation was implemented by [19] for reprojecting the

pixels of a TSI, in the atmosphere cross-section plane, using height measurements acquired using a nearby ceilometer. Ceilometers estimate the height of clouds and have been used to validate low-cost approaches to approximate the height of a cloud using multiple all sky imagers [20, 21]. However, this device is expensive and it is not applicable to more general operations such as a cloud speed sensor [22]. Another low-cost alternative to determine the velocity of clouds moving in the atmosphere cross-section, and thus estimating their heights, was developed using an all sky imager and a grid of sensors (i.e., pyranometers) by [23].

Nevertheless, these geometric transformations were developed for static sky imagers (i.e., TSI and all sky imager). In contrast, the geospatial reprojections introduced in this investigation not only work for static sky imagers, but are also applicable to sky imagers mounted on a solar tracker. In this last case, the perspective in the images is a function of the Sun's elevation and azimuth angles. The first approximation is a reprojection for devices that do not record low elevation angles (see section 3), while the second computes accurate reprojections even when the elevation angle is low (see section 4). The proposed reprojections were originally developed for a low FOV sky imager mounted on a solar tracker [24, 25], however, it is possible to obtain the geospatial reprojection for any FOV and elevation angle by reparameterizing the algorithms. As a ceilometer was not available, the proposed methods were developed so that ceilometer measurements are not required.

2 Rectilinear Lens

The acquired image is the light beam refraction in a converging point of the emitted black body radiation. The image resolution is defined as $N \times M$ pixels. If the radiant objects (the Sun and the clouds) are at a distance $z \rightarrow \infty$, the radiation rays converge at the focal length. Consequently,

$$\frac{1}{f} = \frac{1}{z} + \frac{1}{D} \approx \frac{1}{D}, \quad (1)$$

where f is the focal length and D is the distance from the lens to the converging point. The relation between the diagonal FOV and the focal length f for a rectilinear lens is

$$\tan \frac{\text{FOV}}{2} = \delta \frac{N_{diag}}{2f}, \quad (2)$$

where $N_{diag} = \sqrt{N^2 + M^2}$ is the number of pixels in the diagonal of the sensor and δ is the pixel size. Therefore, the focal length f of camera is,

$$f = \frac{\delta}{2} \frac{N_{diag}}{\tan \frac{\text{FOV}}{2}}. \quad (3)$$

3 Flat Earth Approximation

The *flat* Earth approximation is viable without large error (when the elevation of the Sun ε_0 is higher than 30°) because the portion of the Earth's atmosphere in the FOV of the camera is much smaller than its entire surface. With this assumption, the reprojection from the sensor plane to the atmosphere cross-section plane (in Fig. 1) is obtained with the distance z of a cloud to the camera lens. The distance z is a function of the cloud height h and the elevation angle ε of the cloud in a pixel,

$$z = \frac{h}{\sin \varepsilon}. \quad (4)$$

The reprojection is computed with respect to the coordinates of each pixel i, j in the imager plane. The coordinates of a pixel in the imager plane are defined as $x_j = j\delta$ and $y_i = i\delta$. In this reprojection, we assume that the elevation angle ε_i is different in each row i and constant in each column j of pixels in an image, and the differential angle α_j (formed by the position of Sun and a pixel) is different in each column j and constant in each row i of pixels. This assumption is valid since the FOV of the individual pixels in the rectilinear lens is sufficiently small. As seen in Fig. 1, when intersecting a cloud layer, the projection of the 3D pyramid defined by the camera FOV in a 2D plane forms a triangle. The elevation ε_i and azimuth α_j angles for each pixel i, j are,

$$\begin{aligned} \varepsilon &= \left\{ \left(\varepsilon_0 + i \frac{\nu}{2} \right) \mid \varepsilon_i \in \mathbb{R}^{(0, \pi]}, \forall i = -\frac{N}{2}, \dots, \frac{N}{2} \right\}, \\ \alpha &= \left\{ \left(\alpha_0 + j \frac{\nu}{2} \right) \mid \alpha_j \in \mathbb{R}^{(0, \alpha_x/2]}, \forall j = -\frac{M}{2}, \dots, \frac{M}{2} \right\}, \end{aligned} \quad (5)$$

where $\nu = [\text{FOV}/\sqrt{N^2 + M^2}] \cdot [\pi/180]$ is the camera ratio in radians per pixel, ε_0 is the Sun's elevation angle, and $\alpha_0 = 0$. Therefore, $\alpha_j = 0$ and $\varepsilon_i = \varepsilon_0$ represent the center of the image (since $\alpha_0 = 0$), but only when the number of pixels N and M are odd numbers. For all pixels, ν is approximated by a constant. In this way, the FOV is $\alpha_x = \nu M$ and $\alpha_y = \nu N$ in the x and y axis respectively.

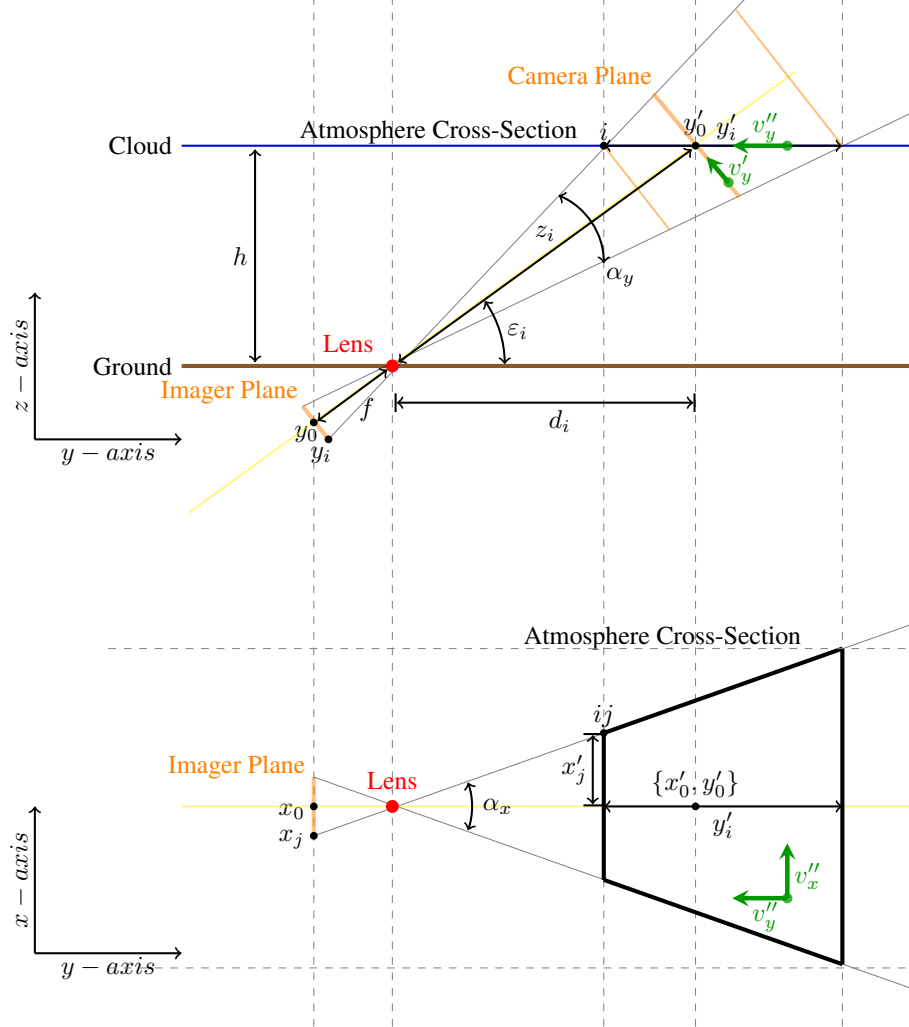


Figure 1: *Flat Earth approximation of the geospatial reprojection.* Top pane (side view): the reprojection depends on the distance z_i of an object to the imager, the height h and the elevation ε_i . Bottom pane (top view): relation of the angular increments α used to compute the elevation angle ε_i of each one of the pixels i, j in the image. The velocity decomposition $\mathbf{v}' = \{v'_x, v'_y\}$ shows that cloud velocity components have a perspective distortion in the x -axis and in the y -axis, due to the camera plane inclination of ε degrees with respect to the normal. x'_j and y'_i represent the coordinates of the pixel in the image (see in Eq. 6). When the coordinate system is centered applying Eq. 20, $\mathbf{x}_0 = \{x'_0, y'_0\}$ represent the origin of coordinates.

The length of a row of pixels j reprojected in the atmosphere cross-section is $x'_{i,j} = x_j \cdot z_i/f$, so substituting z_i in Eq. 4, the coordinates of the imager plane reprojected in the atmosphere cross-section are,

$$\begin{aligned} x'_{i,j} &= \frac{x_j}{f} \cdot z_i = \frac{x_j}{f} \cdot \frac{h}{\sin \varepsilon_i} \\ y'_i &= \frac{y_i}{f} \cdot z_i = \frac{y_i}{f} \cdot \frac{h}{\sin \varepsilon_i}. \end{aligned} \quad (6)$$

4.1 Reprojection of the y-axis

The sagitta ℓ_i of chord C_iD_i is related to the chord AB (Fig. 2). The formula that describes the sagitta ℓ_i is a function of the triangle formed by the intersecting line z_i that goes from AB to C_iD_i with elevation angle ε_i ,

$$\begin{aligned}
\ell_i &= R - \sqrt{R^2 - w_i^2} \\
h - v_i &= R - \sqrt{R^2 - w_i^2} \\
R^2 - w_i^2 &= (w_i \tan \varepsilon_i + r)^2 \\
R^2 - w_i^2 &= w_i^2 \tan^2 \varepsilon_i + r^2 + 2rw_i \tan \varepsilon_i \\
(r + h)^2 &= w_i^2 \tan^2 \varepsilon_i + 2rw_i \tan \varepsilon_i + w_i^2 + r^2 \\
h^2 + 2rh &= w_i^2 (1 + \tan^2 \varepsilon_i) + 2rw_i \tan \varepsilon_i \\
0 &= w_i^2 (1 + \tan^2 \varepsilon_i) + w_i (2r \tan \varepsilon_i) - h(h + 2r),
\end{aligned} \tag{9}$$

where $\ell_i = h - v_i$, $v_i = w_i \tan \varepsilon_i$ and $R = r + h$. The quadratic equation has following coefficients,

$$\begin{aligned}
a_i &= 1 + \tan^2 \varepsilon_i \\
b_i &= 2r \tan \varepsilon_i \\
c_i &= -h(h + 2r).
\end{aligned} \tag{10}$$

The length of triangle side w_i is the result obtained solving the quadratic formula,

$$w_i = \frac{-b_i + \sqrt{b_i^2 - 4a_i c_i}}{2a_i}, \quad w_i \in \mathbb{R}^+. \tag{11}$$

When $r \rightarrow \infty$, $w_i \approx d$ and $v_i \approx h$, thus the *flat* approximation is equivalent to the *great* circle approach $w_i \approx h / \tan \varepsilon_i$.

The *great* circle segment \hat{y}_i is the distance from the center of the arc defined by the saggita ℓ_i to the point D_i (Fig. 2). The chord $2w_i$ is projected to the arc $2\hat{y}_i$ of the *great* circle by applying the arc formula:

$$\hat{y}_i = R \arcsin \frac{w_i}{R}. \tag{12}$$

Each pixel in an image has a different elevation angle ε_i that corresponds to a point D_i in the *great* circle. Therefore, the coordinates of the pixels relative to the imager lens in the atmosphere cross-section plane are calculated subtracting them the distance \hat{y}_{sup} which has the highest elevation (Fig. 3, upper pane),

$$y'_i = \hat{y}_i - \hat{y}_{sup}, \quad \forall i = 1, \dots, N. \tag{13}$$

4.2 Reprojection of the x-axis

The reprojection of the sensor plane x-axis to the atmosphere cross-section is a function of the distance $z_i^2 = w_i^2 + v_i^2$ from the sensor plane to the cloud layer, and the chord $2\hat{x}_{i,j}$ of segment the $2x'_{i,j}$ formed by the angle α_j (Fig. 3, lower pane),

$$\hat{x}_{i,j} = (z_i - \lambda_{i,j}) \tan \alpha_j, \quad \forall i = 1, \dots, M, \quad j = 1, \dots, M. \tag{14}$$

The diameter of the small circle $2s_i$, which is the chord D_iE_i in Fig. 2, is obtained by applying the intersecting chord theorem. In Euclid's Elements Book III, Proposition 35, (see [26]), the intersecting chords theorem is defined as $|AS| \cdot |SC| = |BS| \cdot |SD| = r^2 - d^2$. When this theorem is applied to our problem the corresponding variables are $d = (R - h)$, $r = R$, $|AS| = s_i - z_i$ and $|SC| = z_i$ (see Fig. 2 y-axis graph), so

$$\begin{aligned}
(2s_i - z_i) z_i &= R^2 - (R - h)^2 \\
s_i &= \frac{2Rh - h^2}{2z_i} + \frac{z_i}{2}.
\end{aligned} \tag{15}$$

The relation between the arc length $2x'_{i,j}$ and the chord $2\hat{x}_{i,j}$ is found through the sagitta $\lambda_{i,j}$. The formula which describes

$$\begin{aligned}
(2s_i - \lambda_{i,j}) \lambda_{i,j} &= \hat{x}_{i,j}^2 \\
2s_i &= \lambda_{i,j} + \frac{\hat{x}_{i,j}^2}{\lambda_{i,j}} \\
2s_i \lambda_{i,j} - \lambda_{i,j}^2 &= (z_i - \lambda_{i,j})^2 \tan^2 \alpha_j \\
0 &= \lambda_{i,j}^2 (1 + \tan^2 \alpha_j) - 2\lambda_{i,j} (z_i \tan^2 \alpha_j - s_i) + z_i^2 \tan^2 \alpha_j,
\end{aligned} \tag{16}$$

where coefficients for solving the quadratic formula are,

$$\begin{aligned} a_{i,j} &= 1 + \tan^2 \alpha_j \\ b_{i,j} &= -2s_i - 2z_i \tan^2 \alpha_j \\ c_{i,j} &= z_i^2 \tan^2 \alpha_j. \end{aligned} \quad (17)$$

The sagitta $\lambda_{i,j}$ is the result obtained solving Eq. (16),

$$\lambda_{i,j} = \frac{-b_{i,j} - \sqrt{b_{i,j}^2 - 4a_{i,j}c_{i,j}}}{2a_{i,j}}, \quad \lambda_{i,j} \in \mathbb{R}^+. \quad (18)$$

When $r \rightarrow \infty$, $s_i \rightarrow \infty$, in consequence $\lambda_{i,j} \approx 0$ and $x'_{i,j} \approx \hat{x}_{i,j}$. The *flat* Earth approximation is equivalent to the *great circle* approach.

The arc length $2x'_{i,j}$ is calculated knowing the sagitta $\lambda_{i,j}$ and the small radius s_i ,

$$x'_{i,j} = r'_i \arcsin \left[\frac{(z_i - \lambda_{i,j}) \tan \alpha_j}{r'_i} \right] \quad (19)$$

where segment $x'_{i,j}$ is the projection of x-axis in the atmosphere cross-selection plane.

The origin of the coordinate system can be defined at the position of the Sun,

$$\begin{aligned} x''_{i,j} &= x'_{i,j} - x'_0 \\ y''_{i,j} &= y'_{i,j} - y'_0, \end{aligned} \quad (20)$$

where $\mathbf{x}'_0 = \{y'_0, x'_0\}$ are the pixel index of the Sun position in the image. These equation is applicable to both proposed perspective projections.

5 Results and Discussion

The geospatial perspective projections are applied to a sky imager mounted on a solar tracker that updates its pan and tilt every second, maintaining the Sun in a central position in the images throughout the day. The sky imager is located in the Electrical and Computer Engineering (ECE) department at the University of New Mexico (UNM) central campus in Albuquerque. The climate of Albuquerque is arid semi-continental, with minimal rain, which is more likely in the summer months. The ECE department is approximately located 1, 250m away (i.e., linear distance) from the city center whose elevation is 1, 620m with respect to sea level.

The IR sensor is a Lepton¹ 2.5 radiometric camera with wavelength from 8 to 14 μ m. Pixel intensity within the frame is measured in centikelvin units. The resolution of an IR image is 80 \times 60 pixels. To implement the reprojection, the manufacturing specifications of the camera used are: 63.75 $^\circ$ diagonal FOV, 51 $^\circ$ horizontal FOV_x, 38.25 $^\circ$ vertical FOV_y, and the size of a pixel is $\delta = 17\mu$ m. When other lenses (e.g. fisheye) are used, the camera lens affine projection must first be computed to know the FOV of each pixel.

The pixels in Fig. 4 and 5 are displayed in the camera pixel coordinates (left) and in the atmosphere cross-section plane (right). The pixels are scaled to their actual size in the atmosphere cross-section plane. The distortion produced by the sky imager perspective causes the atmosphere cross-section plane dimensions to increase when the elevation angle decreases.

The difference between both geospatial reprojections is measured using Root Mean Square Error (RMSE). The coordinates computed using the *flat* Earth assumption are $\mathbf{X}_1, \mathbf{Y}_1$, and the coordinates computed using *great circle* approach are $\mathbf{X}_2, \mathbf{Y}_2$. The RMSE, defined as \mathbf{E} , is calculated for each pixel averaging together the difference residuals computed independently in coordinates x and y,

$$\mathbf{E} = \sqrt{\frac{1}{2} [\mathcal{R}(\mathbf{X}_1, \mathbf{X}_2) + \mathcal{R}(\mathbf{Y}_1, \mathbf{Y}_2)]}. \quad (21)$$

The residuals are $\mathcal{R}(\mathbf{X}_1, \mathbf{X}_2) = (\mathbf{X}'_1 - \mathbf{X}'_2)^2$ for each coordinate.

The error maps (see Fig. 6) show the differences between the coordinate systems approximated by both reprojections. The symmetry between both reprojections is not perfectly circular. This is because the elevation angle in *flat* Earth reprojection, was approximated as constant across the pixels in the same row.

¹<https://www.flir.com/>

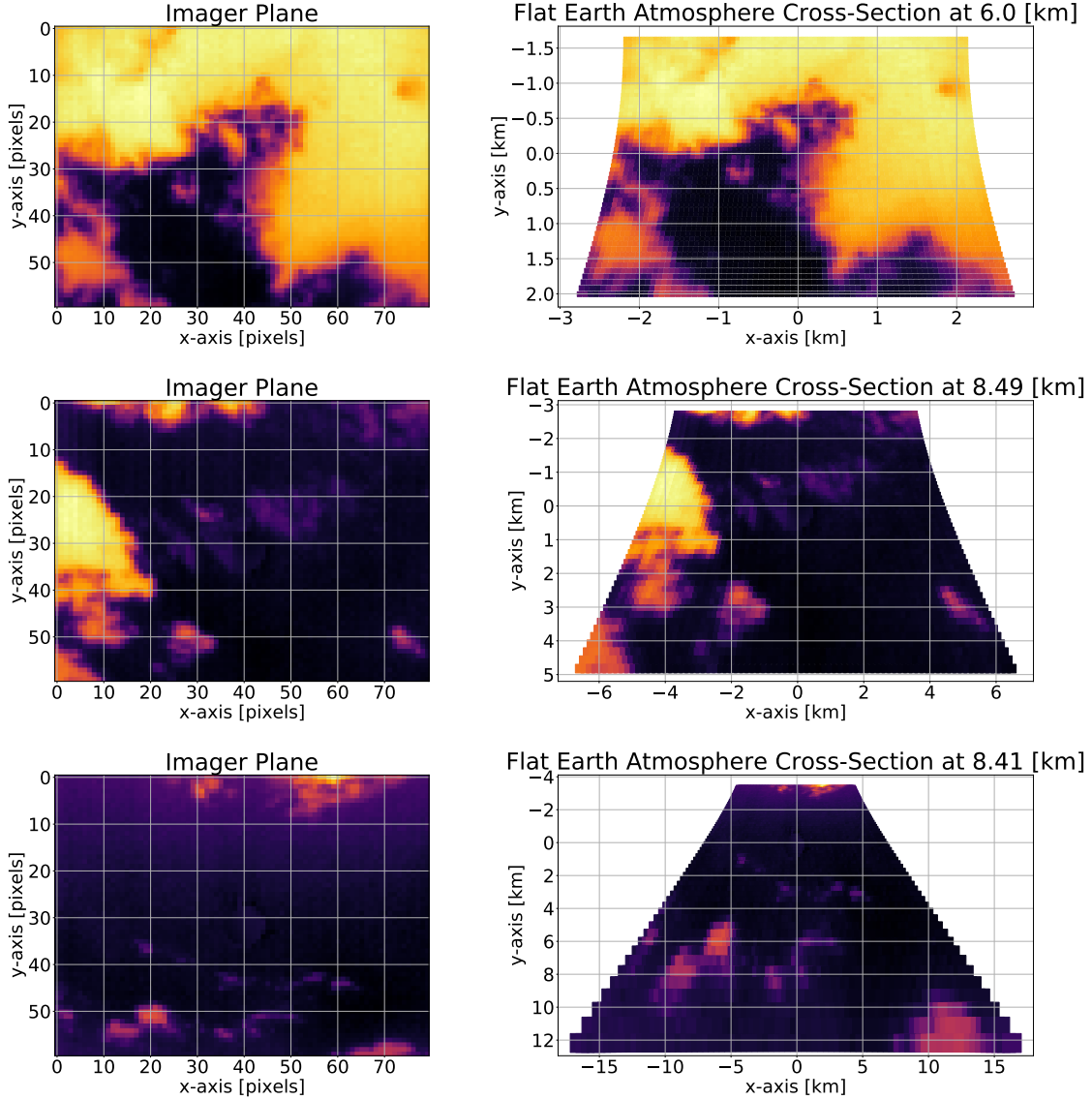


Figure 4: The left column shows three sky images taken at different elevation angles: 71.06° , 50.17° and 30.83° (from top to bottom). The right column shows the same three images after applying the geospatial perspective reprojection using the *flat* Earth approximation.

The tropopause average height is approximately 10km in the latitude where the sky imager is located depending on the season. The first image in Fig. 6 shows the error map when the camera is at the zenith. The magnitude order of the error is in meters when $\varepsilon \geq 30^\circ$. However, when the Sun's elevation angle is below $\varepsilon < 30^\circ$ the magnitude order of the error is in kilometers. Taking this into account, the geospatial reprojection that assumes that the Earth's surface is *flat*, is only adequate when the elevation angle of a sky imager pixel is above $\varepsilon \geq 30^\circ$. If the sky imager is designed to operate below $\varepsilon < 30^\circ$, the most suitable reprojection is computed using the great circle approach.

The difference between both transformations in the magnitude of the error is due to the dimensions of the region of the atmosphere that is being measured with the sky imager (see Fig. 7). As the elevation angle decreases, the region of the atmosphere that is measured in each pixel increases (i.e., perspective). Consequently, the great circle approach performs a more accurate approximation of the cross-section plane of the atmosphere in which the clouds are moving.

The atmosphere cross-section projected on the Earth's surface using the *great* circle approach reprojection is shown in Fig. 8 in Geographic Coordinates System (GCS). The GCS components are longitude and latitude and they are

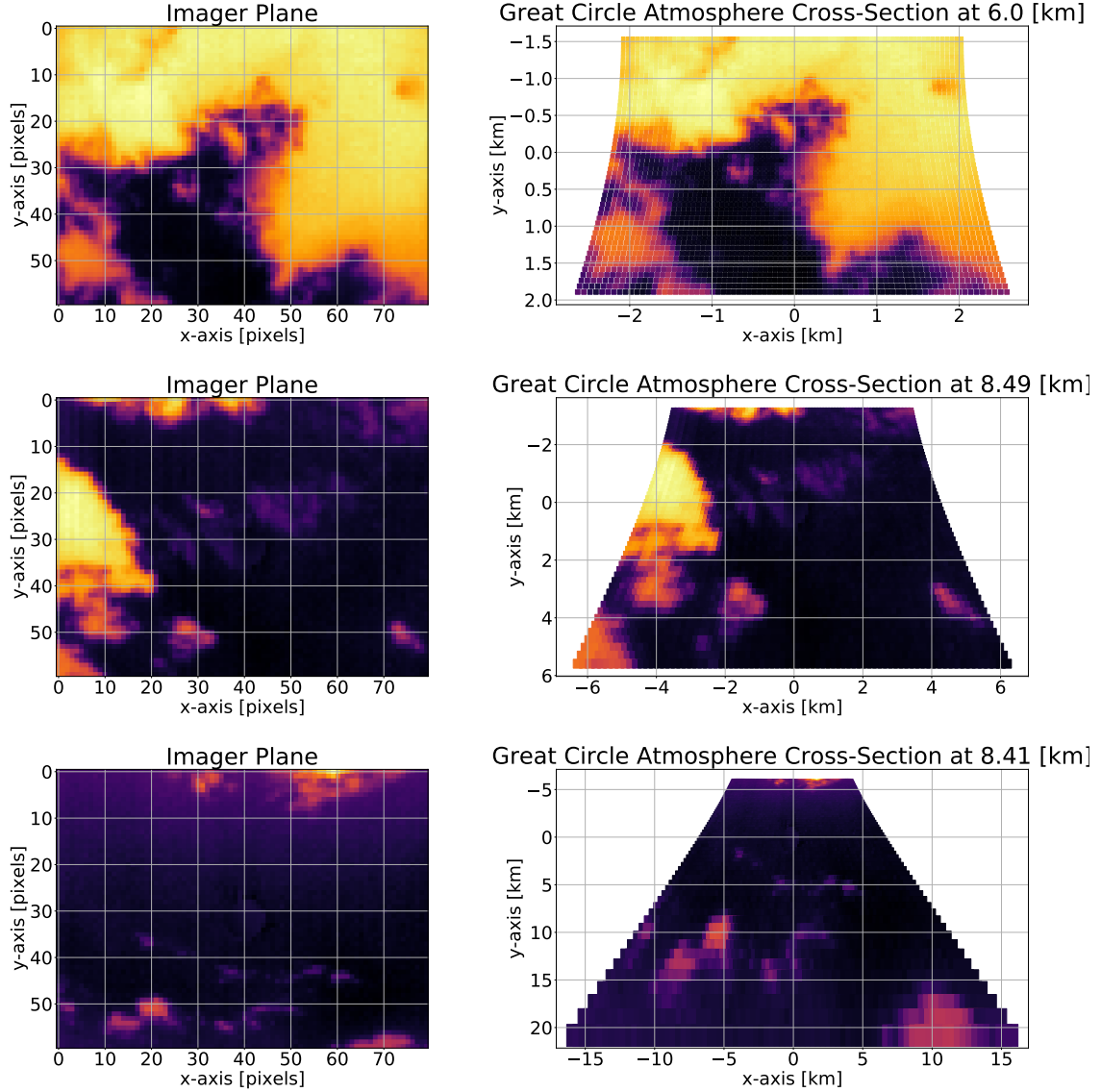


Figure 5: The left column shows three sky images taken at different elevation angles: 71.06° , 50.17° and 30.83° (from top to bottom). The right column shows the resulting sky images after applying the geospatial perspective reprojection using the *great circle* approach.

defined in degrees. The atmosphere cross-section plane is considerably larger when the Sun's elevation angle is low. The distance between pixels in an image increases exponentially from top to bottom.

The results presented in this investigation show that the proposed methodology is advantageous with respect to other methods available in the literature from a theoretical and technological point of view. The geometric reprojection proposed by [27] (i.e., voxel carving) is equivalent to the *flat Earth* approximation investigated in this research, and thus it does not consider the curvature of the Earth (i.e., *great circle* approach). As it is demonstrated in this research (see Fig. 6), the order of magnitude of the error produced by this approximation is in the range of kilometers for high clouds (e.g., stratus) measured by pixels with elevation angles $< 30^\circ$. In addition, low-cost radiometric far infrared cameras provide temperature measurements (e.g., [28]) which can be transformed to height measurements [29] when combined with weather features measured by a simple weather station in the ground [30]. Radiometric infrared cameras have low resolution [24], but their resolution is sufficient to perform accurate intra-hour solar forecasting [31].

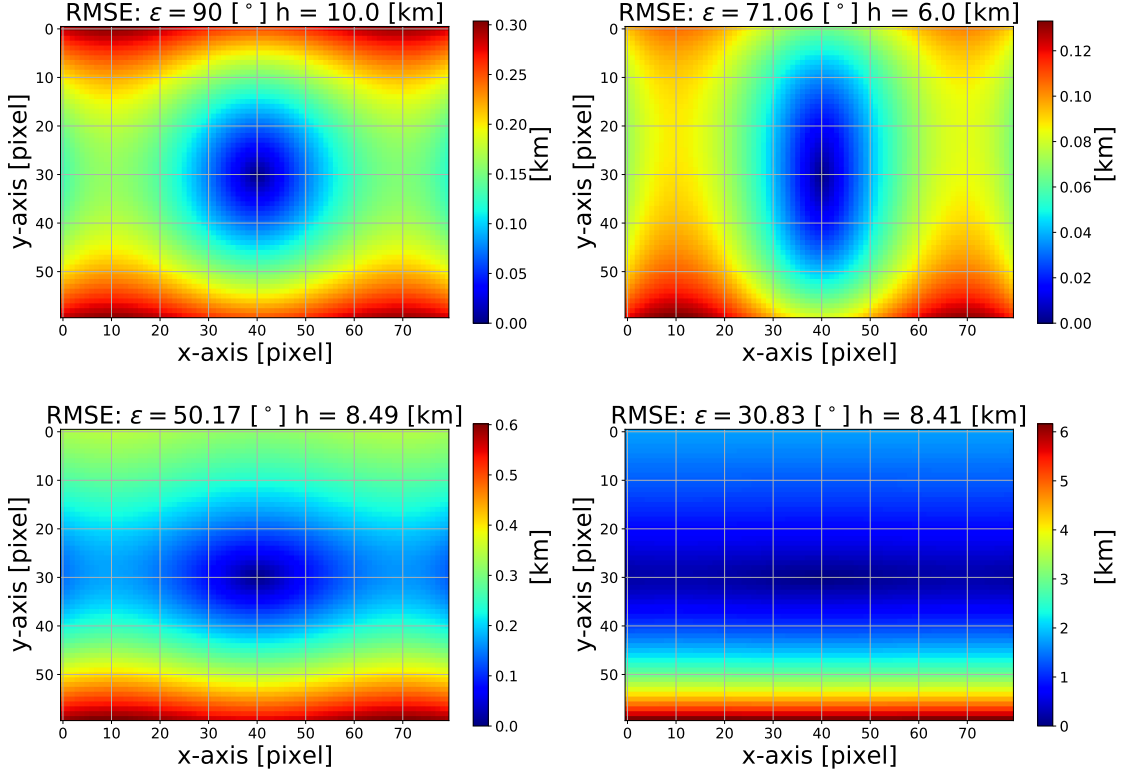


Figure 6: RMSE between the atmosphere cross-section coordinates approximated using the *flat* Earth assumption reprojection and the *great circle* approach reprojection. The coordinates of each reprojection are displayed in Fig. 4 and 5 respectively.

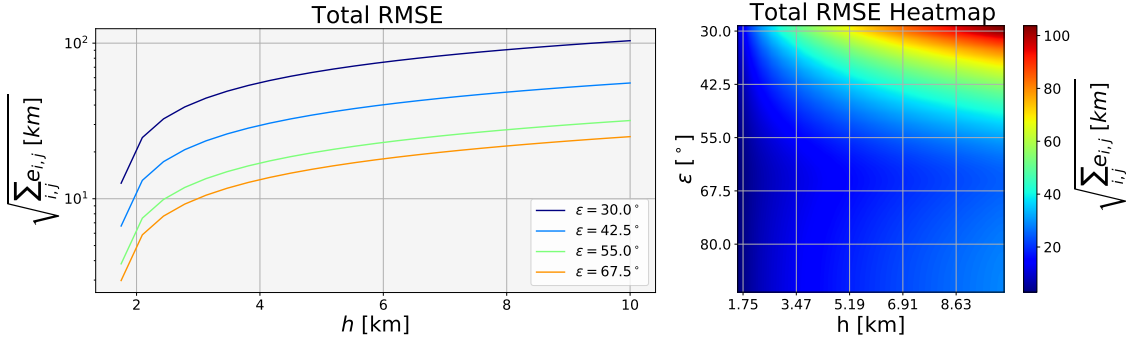


Figure 7: The left graph shows the increase in the quadratic total sum of error as a function of the height for 5 different elevation angles: 30°, 42.5°, 55° and 67.5°. The error function is in Eq. (21). The right graph shows the quadratic total sum of errors as a function of the elevation angle and the height.

6 Conclusion

Intra-hour solar forecasting algorithms utilize consecutive sky images to compute cloud velocity vectors, anticipating when a cloud will occlude the Sun and produce a decrease in the global solar irradiance that reaches the Earth’s surface. Velocity vectors are calculated in units of pixels per frame, but the dimensions of the pixels in sky images vary with the elevation angle. Therefore, the velocity vector accuracy used to forecast cloud occlusions of the Sun can be improved. The proposed perspective reprojection of the sensor plane to the geospatial atmosphere cross-section plane can be used to transform the pixels in sky images to the cross section coordinate system of the clouds.

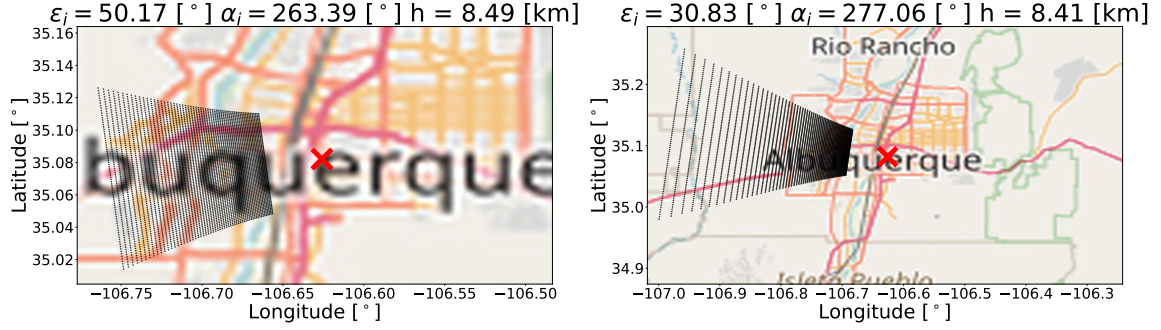


Figure 8: Atmosphere cross-section plane projected on the Earth’s surface for elevations of 50° and 31° . The sky imager localization is the red dot. The sky imager pixels are in black. The coordinates of a pixel are defined by a longitude and latitude angle.

When used in sky imagers, thermal images are advantageous in that cloud height can be approximated when cloud temperature is known. Radiometric infrared cameras composed of microbolometers are an inexpensive technology capable of acquiring thermal sky images. When intersected by the sky-imaging system field of view, the dimensions of the atmosphere cross-section plane can be determined using the proposed reprojections and temperatures of the objects in the images.

7 Data Availability

The procedure to acquire and preprocessing the radiometric far infrared sky images, plus the hardware was described in [24]. The data used in this work is publicly available in a DRYAD repository (<https://doi.org/10.5061/dryad.zcrjdfn9m>). The software for both geospatial perspective reprojections is available in a GitHub repository (https://github.com/gterren/geospatial_perspective_reprojection).

Acknowledgments

This work has been supported by National Science Foundation (NSF) EPSCoR grant number OIA-1757207 and the King Felipe VI endowed Chair of the UNM. Authors would like to thank the UNM Center for Advanced Research Computing (CARC), supported in part by NSF, for providing the high performance computing and large-scale storage resources used in this work. We would also like to thank Marie R. Fernandez for proof reading the manuscript.

References

- [1] P. Tzoumanikas, E. Nikitidou, A.F. Bais, and A. Kazantzidis. The effect of clouds on surface solar irradiance, based on data from an all-sky imaging system. *Renewable Energy*, 95:314 – 322, 2016.
- [2] Weicong Kong, Youwei Jia, Zhao Yang Dong, Ke Meng, and Songjian Chai. Hybrid approaches based on deep whole-sky-image learning to photovoltaic generation forecasting. *Applied Energy*, 280:115875, 2020.
- [3] A. Mammoli, A. Ellis, A. Menicucci, S. Willard, T. Caudell, and J. Simmins. Low-cost solar micro-forecasts for pv smoothing. In *2013 1st IEEE Conference on Technologies for Sustainability (SusTech)*, pages 238–243, 2013.
- [4] Yinghao Chu, Mengying Li, and Carlos F.M. Coimbra. Sun-tracking imaging system for intra-hour dni forecasts. *Renewable Energy*, 96:792 – 799, 2016.
- [5] Guillermo Terrén-Serrano and Manel Martínez-Ramón. Comparative analysis of methods for cloud segmentation in ground-based infrared images. *Renewable Energy*, 175:1025–1040, 2021.
- [6] Chi Wai Chow, Bryan Urquhart, Matthew Lave, Anthony Dominguez, Jan Kleissl, Janet Shields, and Byron Washom. Intra-hour forecasting with a total sky imager at the uc san diego solar energy testbed. *Solar Energy*, 85(11):2881 – 2893, 2011.
- [7] Brian J. Redman, Joseph A. Shaw, Paul W. Nugent, R. Trevor Clark, and Sabino Piazzolla. Reflective all-sky thermal infrared cloud imager. *Opt. Express*, 26(9):11276–11283, Apr 2018.

- [8] M.I. Gohari, B. Urquhart, H. Yang, B. Kurtz, D. Nguyen, C.W. Chow, M. Ghonima, and J. Kleissl. Comparison of solar power output forecasting performance of the total sky imager and the university of california, san diego sky imager. *Energy Procedia*, 49:2340 – 2350, 2014. Proceedings of the SolarPACES 2013 International Conference.
- [9] Ricardo Marquez and Carlos F.M. Coimbra. Intra-hour dni forecasting based on cloud tracking image analysis. *Solar Energy*, 91:327 – 336, 2013.
- [10] Qingyong Li, Weitao Lyu, Jun Yang, and James Wang. Thin cloud detection of all-sky images using markov random fields. *IEEE Geoscience and Remote Sensing Letters*, 9:417–421, 05 2012.
- [11] Chia-Lin Fu and Hsu-Yung Cheng. Predicting solar irradiance with all-sky image features via regression. *Solar Energy*, 97:537 – 550, 2013.
- [12] S. Liu, L. Zhang, Z. Zhang, C. Wang, and B. Xiao. Automatic cloud detection for all-sky images using superpixel segmentation. *IEEE Geoscience and Remote Sensing Letters*, 12(2):354–358, Feb 2015.
- [13] H.-Y. Cheng and C.-L. Lin. Cloud detection in all-sky images via multi-scale neighborhood features and multiple supervised learning techniques. *Atmospheric Measurement Techniques*, 10(1):199–208, 2017.
- [14] Chaojun Shi, Yatong Zhou, Bo Qiu, Jingfei He, Mu Ding, and Shiya Wei. Diurnal and nocturnal cloud segmentation of all-sky imager (asi) images using enhancement fully convolutional networks. *Atmospheric Measurement Techniques*, 12:4713–4724, 09 2019.
- [15] M. Caldas and R. Alonso-Suárez. Very short-term solar irradiance forecast using all-sky imaging and real-time irradiance measurements. *Renewable Energy*, 143:1643 – 1658, 2019.
- [16] M. Hasenbalg, P. Kuhn, S. Wilbert, B. Nouri, and A. Kazantzidis. Benchmarking of six cloud segmentation algorithms for ground-based all-sky imagers. *Solar Energy*, 201:596 – 614, 2020.
- [17] Andrea Mammoli, Guillermo Terrén-Serrano, Anthony Menicucci, Thomas P Caudell, and Manel Martínez-Ramón. An experimental method to merge far-field images from multiple longwave infrared sensors for short-term solar forecasting. *Solar Energy*, 187:254–260, 2019.
- [18] Jaro Nummikoski. *Sky-image based intra-hour solar forecasting using independent cloud-motion detection and ray-tracing techniques for cloud shadow and irradiance estimation*. PhD thesis, University of Texas, San Antonio, 2013.
- [19] Walter Richardson, Hariharan Krishnaswami, Rolando Vega, and Michael Cervantes. A low cost, edge computing, all-sky imager for cloud tracking and intra-hour irradiance forecasting. *Sustainability*, 9(4):482, 2017.
- [20] Dung Andu Nguyen and Jan Kleissl. Stereographic methods for cloud base height determination using two sky imagers. *Solar Energy*, 107:495–509, 2014.
- [21] P. Kuhn, M. Wirtz, N. Killius, S. Wilbert, J.L. Bosch, N. Hanrieder, B. Nouri, J. Kleissl, L. Ramirez, M. Schroedter-Homscheidt, D. Heinemann, A. Kazantzidis, P. Blanc, and R. Pitz-Paal. Benchmarking three low-cost, low-maintenance cloud height measurement systems and ecmwf cloud heights against a ceilometer. *Solar Energy*, 168:140–152, 2018. Advances in Solar Resource Assessment and Forecasting.
- [22] Guang Wang, Ben Kurtz, and Jan Kleissl. Cloud base height from sky imager and cloud speed sensor. *Solar Energy*, 131:208–221, 2016.
- [23] Guang Chao Wang, Bryan Urquhart, and Jan Kleissl. Cloud base height estimates from sky imagery and a network of pyranometers. *Solar Energy*, 184:594–609, 2019.
- [24] Guillermo Terrén-Serrano, Adnan Bashir, Trilce Estrada, and Manel Martínez-Ramón. Girasol, a sky imaging and global solar irradiance dataset. *Data in Brief*, page 106914, 2021.
- [25] Guillermo Terrén-Serrano and Manel Martínez-Ramón. Multi-layer wind velocity field visualization in infrared images of clouds for solar irradiance forecasting. *Applied Energy*, 288:116656, 2021.
- [26] Thomas Little Heath et al. *The thirteen books of Euclid's Elements*. Courier Corporation, 1956.
- [27] Bijan Nouri, P Kuhn, Stefan Wilbert, Natalie Hanrieder, C Prah, L Zarzalejo, A Kazantzidis, Philippe Blanc, and R Pitz-Paal. Cloud height and tracking accuracy of three all sky imager systems for individual clouds. *Solar Energy*, 177:213–228, 2019.
- [28] Peter M Lewis, Howard Rogers, and Rafe H Schindler. A radiometric all-sky infrared camera (rasicam) for des/ctio. In *Ground-based and Airborne Instrumentation for Astronomy III*, volume 7735, page 77353C. International Society for Optics and Photonics, 2010.
- [29] Peter H Stone and John H Carlson. Atmospheric lapse rate regimes and their parameterization. *Journal of Atmospheric Sciences*, 36(3):415–423, 1979.

- [30] Guillermo Terrén-Serrano and Manel Martínez-Ramón. Processing of global solar irradiance and ground-based infrared sky images for solar nowcasting and intra-hour forecasting applications, 2021.
- [31] Guillermo Terrén-Serrano and Manel Martínez-Ramón. Review of kernel learning for intra-hour solar forecasting with infrared sky images and cloud dynamic feature extraction, 2021.